Convergence-free mapping of non-linear damper-blade performance

Original
Convergence-free mapping of non-linear damper-blade performance / Gastaldi, C., Gola, M.M.. - In: MECHANICAL SYSTEMS AND SIGNAL PROCESSING. - ISSN 0888-3270. - 208:(2024). [10.1016/j.ymssp.2023.111062]

Publisher:
Elsevier - Academic Press

Published
DOI:10.1016/j.ymssp.2023.111062

Mechanical Systems and Signal Processing 208 (2024) 111062

Contents lists available at ScienceDirect

Mechanical Systems and Signal Processing

journal homepage: www.elsevier.com/locate/ymssp

Convergence-free mapping of non-linear damper-blade performance

Chiara Gastaldi, Muzio M. Gola *

Department of Mechanical and Aerospace Engineering, Politecnico di Torino, Italy

A R T I C L E I N F O

Keywords:
Nonlinear dynamics
Vibrations
Underplatform dampers
Friction damping
Turbomachinery

A B S T R A C T

In the bladed disks of turbomachinery, the problem arises of finding a damping device that reduces as much as possible the amplitude of the alternating stresses produced by the forced vibrations excited by the gas flow. Dry friction solid underplatform dampers are an established solution.

The shape and size of the damper, in association with those of the platform, neck and airfoil, determine the non-linear response curves having as parameter the intensity of external excitation, here synthetically represented by a “proof” excitation force. Of greatest importance are the combinations (frequency, excitation force) that realise the maximum amplitude of forced oscillation (measured, for example, at the blade tip) and the maximum value of the amplitude of the variable stress produced by the vibrations at a critical point of the blade. Since the design of the damper-blade coupling is High-Cycle Fatigue driven, this stress amplitude is taken as a reference and related to the value of the excitation force. This can finally take the well-known form of the damper performance curve.

Especially in the case of parametric explorations concerning shape, size and contact parameters, the current approach to this non-linear response problem, based on iterative convergence, is numerically prohibitive unless one uses special search techniques, such as the surrogate models of various types that are favoured today.

An alternative computational process is presented here, that of integrating PCR (Platform Centred Reduction) with a new approach called Amplitude Layered (excitation) Force Mapping. This process reduces the amount of computation by up to three orders of magnitude compared to standard techniques and is a winning alternative to surrogate models.

1. Introduction

Friction dampers are used in turbomachinery to reduce resonant stresses in turbine blades by providing controlled contact between points that undergoing relative motion due to vibration dissipate resonant vibration energy. Underplatform dampers (UDs) are in contact with the platforms belonging to two facing blades. The platforms together with the UDs create a circumferential continuity that separates the flow-path of the working gas flowing through the airfoils at the top, and the flow-path of the air cooling blade neck and disk rim.

The main design criterion for UDs is to determine the shape and mass of the damper that best matches a given blade to reduce blade

---

* Corresponding author.
E-mail address: muzio.gola@polito.it (M.M. Gola).

https://doi.org/10.1016/j.ymssp.2023.111062
Received 19 July 2023; Received in revised form 1 December 2023; Accepted 18 December 2023
Available online 31 December 2023

Nomenclature

Main Symbols

u, v, w	rigid body displacements
α, β, γ	rigid body rotations
k_{Re}	real part of the complex spring representing the damper
k_{Im}	imaginary part of the complex spring representing the damper
$M_{\gamma,P}$	Equivalent moment produced by the contact forces on point P of the platform
$\mathbf{D}$	dynamic stiffness matrix
$\mathbf{M}, \mathbf{C}, \mathbf{K}$	mass, damping and stiffness matrices
h	harmonic index
ω	frequency in rad/s
$\mathbf{q}$	vector of displacements
$\mathbf{f_E}$	vector of external forces
$\mathbf{f_C}$	vector of contact forces
R, $\mathbf{R}$	Residual of the iterative, convergence-based nonlinear calculation. Depending on the approach, the residual may be a scalar or a vector
F_E	Amplitude of the external forces vector
γ_P^*	Platform rotation amplitude
$\sim \gamma_P^*$	Response curve obtained with $F_E = 1$ N at a constant value of complex stiffness $k_{Re}(\gamma_P^*) + ik_{Im}(\gamma_P^*)$ corresponding to γ_P^*
A	Maximum point of a γ_P curve
Z	Any other point (not a maximum) of a γ_P curve
f	Frequency in Hz
F_{lim}	Limit value of the external force above which the amplitude of the response becomes bounded only by structural damping (i.e. friction damping ceases to be effective)
σ_a	alternating stress amplitude at the airfoil-plaftorm junction
$\sigma_{a,all}$	allowable alternating stress amplitude

Additional superscripts and operators

Q^h	h-th harmonic order of a quantity expressed in the frequency domain
${}^xQ$	Quantity obtained by imposing a $F_E = x$
$\sim Q^*$	Quantity obtained by imposing a constant value of complex spring $k_{Re}(\gamma_P^*) + ik_{Im}(\gamma_P^*)$ corresponding to γ_P^* regardless of the actual value of the platform rotation

stress as much as possible.

As far as contacts are concerned, the common technique today is to connect each pair of nodes facing each other on two contact surfaces with a “spring-slider” element, sometimes also referred to as a “Jenkins” element, which is fully characterised by normal and tangential stiffnesses and a Coulomb dry friction law. In the context of this and related work preceding it, it is considered that the contact parameters (k_n, k_t, μ) can be calibrated through measurable physical properties of the contact forces [1–4].

With regard to the type of damper, it is surprising that after so many years there is no agreement on the fundamental point of its shape. Even in the last few years, studies continue to be proposed that use, among the prismatic solid dampers, the ’cottage-roof’ or ’wedge’ type [5–9], which can never guarantee a stable contact at both interfaces with the adjacent platforms, because it is not self-aligning and therefore cannot absorb angular tolerances and misalignments. Neither can it absorb time-varying non-parallelism between the surfaces of the two adjacent platforms, obviously in the case of Out-of-Phase vibration, but also in the case of In-Phase vibration when the Interphase angle is not zero. When, on the contrary, the asymmetrical contact damper [10,11] is proven [12] to allow self-alignment in all possible cases.

There are other differences in approach that should be understood as opportunities for constructive debates and cross fertilization between research groups. One is the choice of the most appropriate number of contact points to be introduced into the model of a contact area or line. Another is to assure the proper bedding of the UD on the platform through pads placed at the outer edges of the available plane-on-plane contact area [12], as a preventive measure against surface shape imperfections [13] or to better comply with the predictable pattern of in-service wear [14].

All of this has a bearing on the numerical size of the model, which today usually boasts millions of nodes and tens of millions of degrees of DOFs. Of these, the vast majority are ’linear’ DOFs, i.e., which will not be the site of application of non-linear forces, while a few dozen to up to a few hundred may be contact nodes, potentially non-linear. With the exclusion of some external force application points and some points witnessing the blade displacements, linear DOFs are condensed by expressing them as a function of contact DOFs. Consequently, most non-contact DOFs are excluded from the equations. However, full accuracy is preserved, while the size of the system to be solved through HBM is limited just by the highest harmonic order and the number of contact DOFs. Strategies are available to solve the efficiency vs. accuracy trade-off of harmonic selection for nonlinear systems [15]. However, it turns out that for well-behaved dampers the Harmonic order does not need to be higher than one [15].

In this context, at first glance, it would seem of limited interest to drastically reduce linear DOFs through the adoption of rigid-body models for damper and platform, as proposed here through the PCR method (presented in [16–18], brief description in Chapter 2). However, it should not be overlooked that this results in a drastic reduction in nonlinear DOFs, which is accompanied by a concomitant greater efficiency in the convergence of the iterative process of calculating the solution due precisely to the smaller number of variables [16–18].

One of the most focused tasks in research on damping of turbine blade systems today is the optimisation of damper and platform geometry, towards the most effective damper-blade matching, in the presence of both uncertainties in geometry and variability in contact parameters.

This poses new challenges. It becomes necessary to keep the computation time well below the values, considered prohibitive, found in computationally intensive problems when one wants to systematically explore a design space. Symptomatic examples are:

- [19] discusses a probabilistic approach (robust design vs. localised optimisation) to consider the effect of contact parameters, which are often difficult to determine and a source of uncertainty; the combination of non-linearity, large size and reliability assessment entails "*prohibitive computational costs*", unless drastically reduced order models (ROM) are used; a ROM based on the concept of non-linear modes is used for this purpose; the demonstration is made on a simplified model which the authors themselves amiably call "*a caricature of a realistic geometry*" (it includes a rigid-body UD), but we argue here (on the basis of the PCR concept defined in Chapter 2) that the same number of non-linear DOFs can be, instead, perfectly realistic.
- [20] a blade-damper coupling analysis is done in a design space defined by ten (however, geometric only) parameters, of them three for the damper (modelled by FEA but keeping just the rigid body degrees of freedom); two "surrogate models" are introduced and compared, both of them capable of reducing by several order of magnitude the computing time otherwise required by a regular DOE factorial sampling; here too the UD is modelled as a rigid body.
- [7] addresses the "*damping performance, resonance frequency stability and robustness … independent of typical manufacturing tolerances*" of a symmetrical wedge damper (however extendable to other shapes), a "proof-of-concept" on a geometry based on academic test rig; high-order modelling of the contact interfaces, in combination with a surrogate model, is proposed to make the computation time addressable when optimizing the UD.

This contribution ideally concludes the work carried out by the authors in recent years, conducted from state-of-the-art strategies (component-mode synthesis, multi HBM and reduced-order modelling) but gradually introducing all those reductions in the complexity of the problem that would make it tractable for the purpose of damper-blade coupling optimization without sacrificing the accuracy of the results.

This methodological program was gradually developed within a well-defined area of engineering interest: self-aligning dampers with asymmetrical contacts, rigid-body models for platform and damper, use of the Platform Centred Reduction (PCR) technique, optimization of the damper-blade coupling in the first bending mode, low engine-order excitation (i.e., blades vibrating almost In Phase), equilibrium equations represented in the frequency domain (i.e., HBM), pre-optimized shape of the damper [21] that correctly captures the effects of contact nonlinearity already with the harmonic order of 1.

The completion, presented here, of the previous work consists in a process of direct (excitation) Force Mapping that eliminates the iterative convergence to the solution of the non-linear response and, of course, the associated Jacobian.

The work is organized as follows. Sections 2 and 3 recap basic concepts previously introduced such as the PCR technique and the Base-Cycle, with the related form taken by the state-of-the-art convergence-based numerical methods ordinarily used to solve the nonlinear equilibrium equations. Section 4 introduces the concept of 'Convergence-free', 'Amplitude Layered', Force Mapping of the non-linear response, that is the focus of this paper. Its validation against standard convergence-based numerical methods is also presented. The results are compared with those obtained in a previously published work by the same authors, and the savings in computational effort are estimated circumstantially. Conclusions, in Section 6, summarize the merits and range of validity of the method presented here or the first time.

2. Background

This paper concerns the non-linear dynamic solution of disk-mounted turbomachinery blades, excited to vibrate In-Phase (IP), equipped with UDs that interact with the blade platforms through contact areas, the interaction being represented by dry-friction stick-slip contact elements.

The background of many years of studies, both numerical and experimental, conducted by the authors within the AERMEC Laboratory of the Polytechnic University of Turin, culminates most recently in the proposal of computational methods that, by grasping the essentials, have been able to drastically reduce the numerical burden of damper-blade coupling optimization, while facilitating the interpretation of results.

The characterizing developments proposed by the authors are summarized below.

In a nutshell, a series of off-the-beaten-path developments first showed that the number of nonlinear degrees of freedom, on which the complexity of the dynamic solution depends, can be drastically reduced to that of rigid bodies, that is, to a maximum number of 6 for both the platform and the damper. After this, it was shown that the mode of vibration for which the damper is largely the most effective, Mode 1, can be studied as plane motion by considering (for damping purposes) a single angular rotation of the platform and by formulating the interaction of the platform with the two adjacent dampers by means of a nonlinear complex moment, a function of that rotation angle.

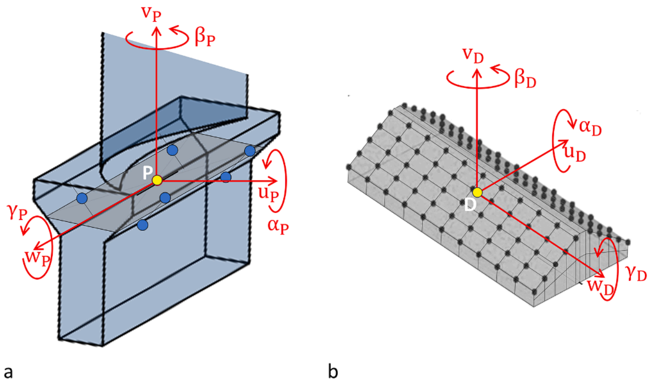

Fig. 1. a) Platform's rigid body rotations α_P, β_P, γ_P; minimum number of 3D contact points for asymmetric-contact dampers (from [17] adapted). b) UD's rigid body rotations α_D, β_D, γ_D; cottage-roof damper with a high number distributed contact points (from [9] adapted).

At the end of this process of reasoned simplification, the damper is dematerialised, i.e. it no longer appears as a physical body participating in the dynamic calculation and, on the contrary, is represented by a rotational stiffness applied to a single axis of the platform. Such stiffness being a complex function of the angle of rotation around that axis, which can be calculated a priori once the geometric shape of platform and damper and their contact parameters have been given.

The authors wish to emphasize that the method used during these developments was always critically attentive to numerical-experimental validation of the numerical results from the FE-MHBM against those from the innovative methods as they were introduced.

In paper [21] on damper pre-optimisation, standard full FE-MHBM was applied to a two-blade laboratory test-rig, accurately cross-checking numerical results with their experimental counterpart.

During the development of the PCR (ref. to section 2.2) [16] showed a comparison between the PCR model and the full FE-MHBM applied to blades with realistic airfoils:

- by cross-checking displacements at sensitive witness points of airfoil and platform, both in static and in modal analysis.
- by comparing displacement response curves from the full FE-MHBM to those from the PCR model, at the three airfoil witness points for two excitation levels corresponding to full-stick and full non-linearity.

This was done as well in [18] (ref. to section 2.3), this time with a comparison of forced responses between a standard full FE MHBM and the "PCR + Base Cycle" method proposed there for a blade under three excitation levels, all in the non-linear domain.

It should be noted that the efforts outlined above were intended to aid designers during the early stages of the design process, where exploring a wide range of potential design solutions may be necessary. In [17] the close link between "PCR + base cycle" and "full FE-MHBM" methods was discussed in detail to showthat the former can be used to identify the optimized blade–damper configuration, then, the latter is used to screen it. With an added advantage that once non-linear contact forces have been calculated with the PCR in a desired number of cases in the range if interest, they can be fed ex-post into the full FE model together with the corresponding excitation forces and frequencies. At this point the solution will be a linear one for each case, enabling the determination of displacements and stresses at all points on the blade for final certification purposes. It was stressed in [17] that the aim is not to substitute full FE calculations but rather to judiciously employ them, limiting their application to the conclusive stage of the design process.

In greater detail.

2.1. *The platform centred reduction to rigid body DOFs [16,22]*

The platform (between the blade neck and the airfoil) on the one hand is traversed – through its radial cross-sections – by forces and moments between the blade neck and the airfoil, and on the other hand receives contact forces from the adjacent dampers.

In [16,22] it was observed that the shape and dimensions of the platform are such that it behaves substantially as a rigid body joining the neck and airfoil, which in comparison are much more deformable. At the same time, deformations in the damper due to contact forces are also orders of magnitude smaller than those due to rigid body kinematics.

It was concluded that platform and damper can be selectively described – without loss of fidelity – by the kinematics of rigid bodies, i.e. by three displacements and three rotations according to three axes located at the appropriate points, and that the normal and tangential contact forces can be reduced to three force components and three moment components along and about such axes. It follows that whatever the number of contact elements one wishes to consider, from a few units [3] up to several tenths or hundreds [6,8], Fig. 1a and b, what counts are the six non-linear forces and moments on the platform and damper.

This gave rise to the proposal of the PCR, Platform Centred Reduction, as a method of drastically reducing the non-linear degrees of freedom of the coupled blade-damper problem [16].

Fig. 2 pictorially summarises the PCR concept.

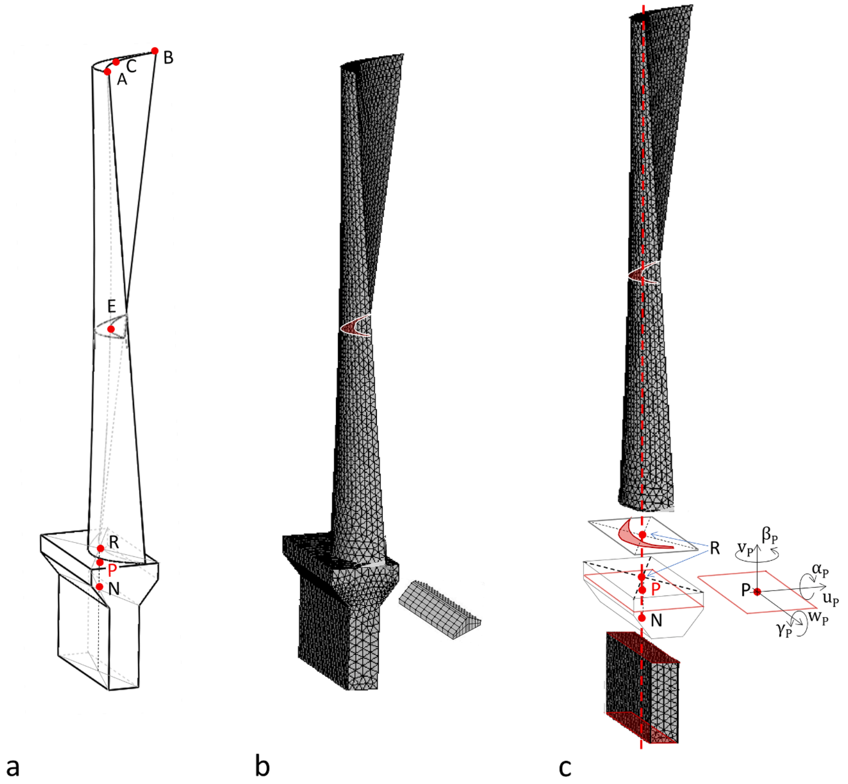

Fig. 2. a) blade body shape and main reference points. b) full FEM blade and damper model. c) concept of the PCR – Platform Centred Reduction.

Fig. 2a represents the external shape of the neck/platform/airfoil assembly. The blade is represented starting from the neck, upwards. While recognizing the importance of blade-disk attachment, this study focuses specifically on optimizing the damper-blade coupling. To streamline the analysis and maintain a manageable scope, considerations such as additional damping from disk attachment interfaces have been intentionally excluded here, as the primary objective is the optimization of the damper-blade coupling. However, there is no impediment in introducing a blade-disk attachment model to account for additional (modest) damping and elastic constraint on the blade neck. Points A, B, C are used as witness points to track the accuracy of the displacements, especially in the first three modes.

Point E is used as a "proof" excitation point, i.e. a point where the equivalent aerodynamic force F_E, representing the integral of the gas pressure fluctuations on the whole airfoil, is applied. Here the location of point E was chosen at the airfoil mid-length. The pair (E, F_E) is used as a comparative criterion for functional tests.

Point R lies on the airfoil/platform separation plane, while point N lies on the platform/neck plane. Point P is an appropriate point on the platform located, as are R and N, on the radial axis of the neck.

Fig. 2b shows the standard "high fidelity" FEM model of the blade assembly, together with one of the two adjacent dampers, which is also FEM modelled. The dots on the side surfaces show a possible choice of positions for the damper-platform contact points.

Fig. 2c shows the PCR model, where the platform is modelled as a rigid body whose displacements depend, at each point, on those of a plane orthogonal to the radial axis containing the point P, and thus completely governed by the three displacements (u_P , v_P , w_P) and the three rotations (α_P , β_P , γ_P). The damper, not represented, is treated in a similar way.

The PCR can be understood as an exemplary case of "selective fidelity", as the internal relative displacements between both platform and damper points – due to contact forces – are completely negligible compared to the absolute displacements of both, thus playing an absolutely irrelevant role in determining the relative kinematics at the contacts. On the other hand, any claim of greater accuracy with a FEM platform compared to rigid body kinematics would have to contend with the fact that the very expedient of modelling contacts between surfaces with a distribution of Jenkins elements is, anyway, a simplification of contact reality.

A similar "selective fidelity" argument applies to the attachment of the lowest cross section of the airfoil to the platform, as if it were constrained to a rigid plane. As well as to Mode 1 platform kinematics, where only the rotation γ_P of the platform in the frontal plane is considered, the other two rotations α_P, β_P being comparatively negligible (Fig. 2c).

2.2. The further reduction to a plane motion in Mode 1 [16,17,18,22]

The elongated rectangular shape of the neck cross-section, where the largest dimension is a multiple m ($m > 1$) of the smallest dimension implies that the ratio of the two bending area moments of inertia lie in the ratio m^2, what under the Mode 1 excitation

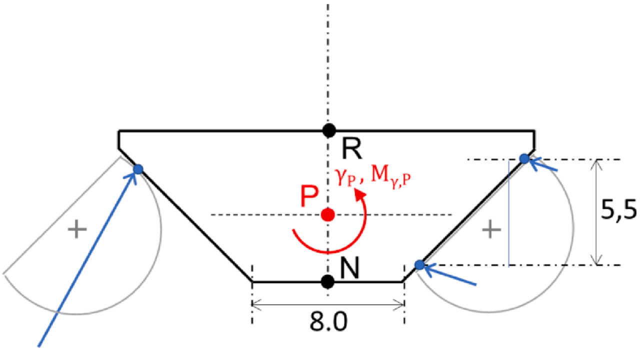

Fig. 3. Main data of the here employed plane platform model, with minimum number of contact points on an asymmetric damper.

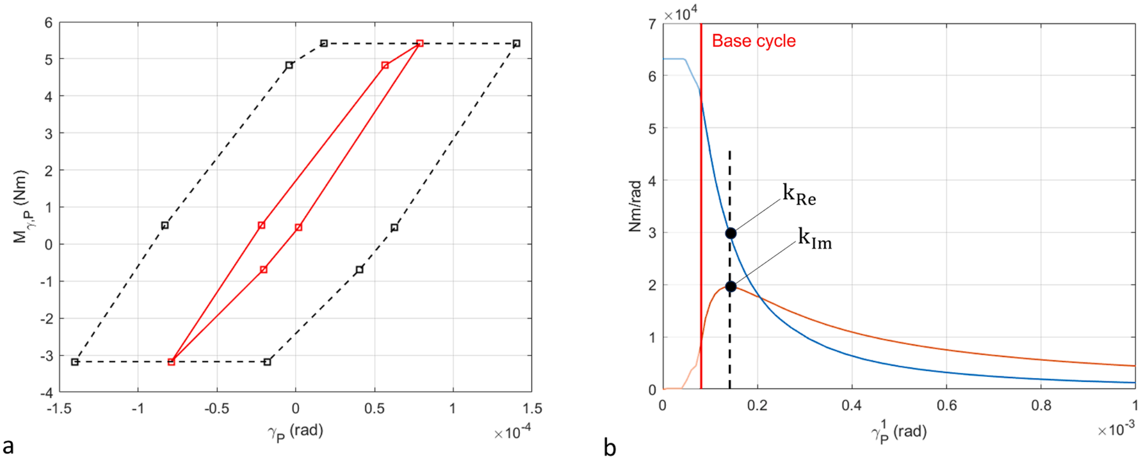

Fig. 4. a) base-cycle (red) and a sample elongated one (black). b) first order HBM real and imaginary components of the damper-to-platform rotational stiffness. (For interpretation of the references to color in this figure legend, the reader is referred to the web version of this article.)

conditions makes biaxial neck bending practically negligible [18,22].

In [16] a realistic twisted and tapered profile was introduced, and in [17] it was shown for two blade dimensions that although the profile has significant flexural-torsional coupling, in Mode 1 the motion of the platform would be predominantly in the (frontal) plane orthogonal to the uniaxial bending axis of the neck. The value of the “limit excitation force” calculated from the energy balance under the assumption that the moments and forces on the platform were reducible to only the frictional moment in the frontal plane was consistent with the position of the asymptote of the force response calculated with the FEM.

In [18] data were provided for rotations, displacements and moments on the platform of the largest blade, derived from the calculation (FEM) of the forced response at two levels of excitation: the lowest with the damper in stick (linear behaviour) and the highest at a value that produces full slip (nonlinearity) at about 50 percent of the asymptotic limit of the excitation force.

In Mode 1 (first bending), the platform rotation in the frontal plane was of order 10^2 greater than the simultaneous torsion angle about the radial axis and of order 10^4 greater than the bending rotation in the plane orthogonal to the frontal plane.

In contrast, for Modes 2 and 3 (second bending, torsion) this was no longer true, since two of the three angles wereof the same order of magnitude. The rotations of Modes 2 and 3 decrease by one/two orders of magnitude compared to those of Mode 1: this proportionally compromises the effectiveness of the damper.

In conclusion, the γ_P (Figs. 1 and 2c) rotation predominates over all others in Mode 1, making the model with plane motion for the platform and damper a fully legitimate engineering practice. Moreover, Mode 1 is the one for which the damper has the highest effectiveness, and thus is the target for optimisation. In contrast, the effectiveness of the underplatform damper for Modes 2 and 3 is very limited as far as damping is concerned, while it definitely plays a role on the coupling between adjacent blades through contact stiffness.

2.3. The HBM complex stiffness and the Base-Cycle [12,18]

The relationship that exists between the γ_P rotation and the $M_{\gamma,P}(\gamma_P)$ moment produces the hysteresis loop which summarizes the joint effect on the platform of all the stick-slip contact points.

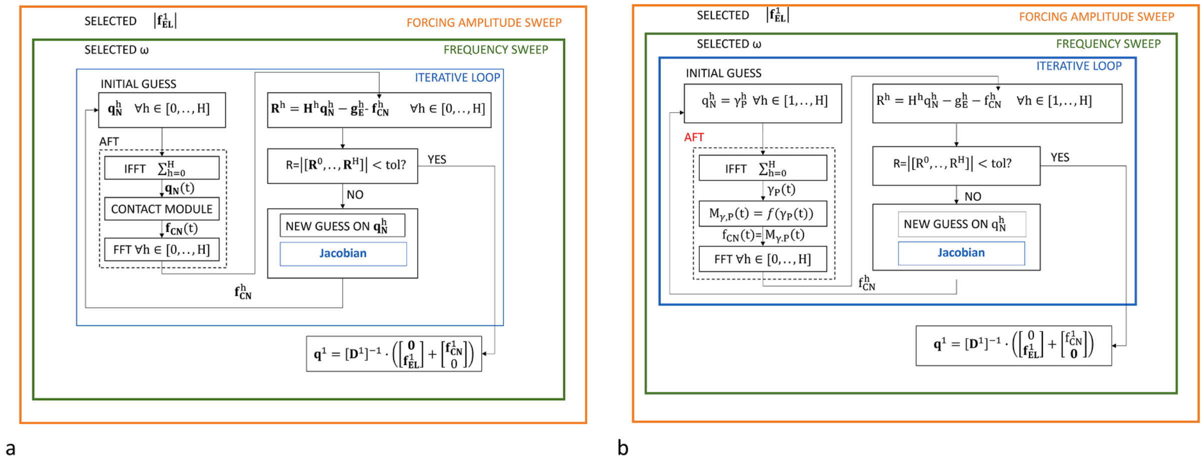

Fig. 5. a) the nesting of the iterative loop for both the standard MHBM full FEM and the 3D PCR. b) the nesting of the iterative loop in 2D (plane), 1 DOF (plane) PCR for Mode 1, In-Phase.

In the traditional method, a frequency-time step (AFT: Alternate Frequency Time) is performed at each convergence cycle to calculate the contact forces during the cycle for a given amplitude. However, in the case of PCR reduced to plane motion it is possible to know beforehand the real imaginary stiffnesses as a function of the rotation amplitude only, and therefore the calculation of the cycle shape can be extracted outside the iterative calculation.

This opportunity is further enhanced by the observation that the "Base-Cycle" of the damper-platform system can be calculated once and for all, i.e. the cycle established at the smallest amplitude in which all the contacts reach the slip condition [18]. The calculation of the Base Cycle is done with high accuracy and negligible computational effort either as is in [12] or with the time marching algorithm of [23]. For each cycle of greater amplitude, the ascending and descending sections of the cycle remain unchanged, while it lengthens in rotation at constant maximum and minimum moments. Therefore, its HBM expression, with the corresponding stiffness, can be calculated in a trivial way for any amplitude greater than that of the Base-Cycle. Thus, the function of the type represented in Fig. 4b is obtained (Fig. 3, Appendix A).

The consequences of all these steps are:

- the relative damper-platform movements occursin planes parallel to the frontal plane, so that their moment component about the axis orthogonal to the frontal plane largely prevails over the components about the other two axes.
- the platform rotation γ_P and the moment due to contact forces, $M_{\gamma,P}$, both about the axis orthogonal to the frontal plane, Fig. 3, are HBM related to the first harmonic order by means of a complex spring ($k_{Re} + i\, k_{Im}$), a function of rotational amplitude γ_P^1, predetermined on the basis of damper and platform parameters.
- the damper has become" immaterial" in the sense that its physical model no longer appears in the dynamic calculation and is replaced by the aforementioned equivalent complex stiffness as a function of rotational amplitude γ_P^1, predetermined on the basis of the damper and platform parameters.

A further proof of the validity of the techniques described in Sections 2.1 to 2.3 is given in Section 3, where the nonlinear response computed using state-of-the-art full FE, 3D PCR and 2D PCR are compared.

3. The Newton-Raphson convergence of the non-linear response

The traditional approach to the numerical computation of the non-linear response of damped blades starts with the expression of the dynamic equation into the frequency domain:

$$\mathbf{D}^h\mathbf{q}^h = \mathbf{f}_E^h + \mathbf{f}_C(\mathbf{q})^h \qquad \forall h \in [0, H] \tag{1}$$

where $\mathbf{D}^h = -(h \bullet \omega)^2\mathbf{M} + i \bullet (h \bullet \omega)\mathbf{C} + \mathbf{K}$ is the dynamic stiffness matrix, a function of the mass $\mathbf{M}$, damping $\mathbf{C}$ and stiffness matrices $\mathbf{K}$, $\mathbf{f}_E^h$ is the vector of the external forces and $\mathbf{f}_C(\mathbf{q})^h$ is the vector of contact forces. The variable h represents the harmonic index which spans the range $[0, H]$, where $h = 0$ represents the static calculation and H represents the maximum harmonic index used in the calculation ($H = 1$ for simple HBM and $H > 1$ for MHBM)

Eq. (1) is then partitioned into nonlinear (subscript N) and linear (subscript L) DOFs, as detailed in [24].

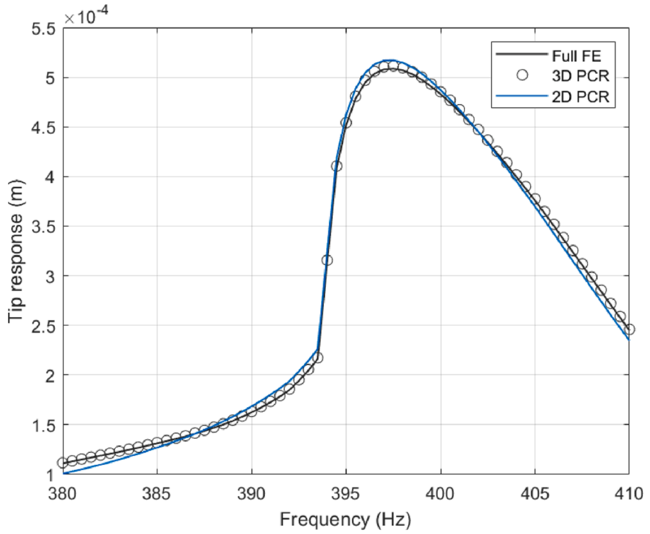

Fig. 6. Comparison of the nonlinear blade tip response for MHBM Full FE (state-of-the-art), 3D PCR and 2D PCR, excitation force $|\mathbf{f}_{EL}^1| = F_E = 5$ N.

$$\begin{bmatrix} \mathbf{D}_{NN}^h & \mathbf{D}_{NL}^h \\ \mathbf{D}_{LN}^h & \mathbf{D}_{LL}^h \end{bmatrix} \begin{bmatrix} \mathbf{q}_N^h \\ \mathbf{q}_L^h \end{bmatrix} = \begin{bmatrix} \mathbf{f}_{EN}^h \\ \mathbf{f}_{EL}^h \end{bmatrix} + \begin{bmatrix} \mathbf{f}_{CN}^h(\mathbf{q}_N^h) \\ 0 \end{bmatrix} \tag{2}$$

Since linear DOFs can be expressed as a function of the DOFs where non-linear contact forces act, Eq. (2) can be restated in terms of such non-linear DOFs. :

$$\mathbf{H}^h \mathbf{q}_N^h = \mathbf{g}_E^h + \mathbf{f}_{CN}^h(\mathbf{q}_N^h) \qquad \forall h \in [0, H] \tag{3}$$

where

$$\begin{aligned} \mathbf{H}^h &:= \mathbf{D}_{NN}^h - \mathbf{D}_{NL}^h \left(\mathbf{D}_{LL}^h\right)^{-1} \mathbf{D}_{LN}^h \qquad \forall h \in [0, H] \\ \mathbf{g}_E^h &:= -\mathbf{D}_{NL}^h \left(\mathbf{D}_{LL}^h\right)^{-1} \mathbf{f}_{EL}^h + \mathbf{f}_{EN}^h \end{aligned} \tag{4}$$

The full process to obtain the nonlinear forced response for selected values of frequency and levels of excitation is detailed in Fig. 5a.

Inside the AFT (Alternating Frequency Time) procedure box, the sum of vectors $\mathbf{q}_N^h$ is converted from the frequency domain to the time domain $\mathbf{q}_N(t)$. In the standard procedure, $\mathbf{q}_N(t)$ is partitioned into the portions pertaining to the different contact pairs. The contact model is then run for n_C times (the number of contact points) to produce the corresponding contact forces which will be used to build the vector of contact forces $\mathbf{f}_{CN}(t)$, which is then converted back to the frequency domain $\mathbf{f}_{CN}^h$.

The 3D PCR version [16] is formally the same as the scheme in Fig. 5a, except that the platform and damper are governed by $\mathbf{q}_N(t)$ in the number of 12 rigid-body displacements and rotation, 6 each, acting as non-linear variables. The n_C time-displacements of contact points are expanded through a matrix transformation of time-displacement vector $\mathbf{q}_N(t)$. The contact forces determined for each time step are then matrix recombined into the vector rigid body resultant forces and moments $\mathbf{f}_{CN}(t)$, then converted back to the frequency domain $\mathbf{f}_{CN}^h$.

In the 2D (plane) "Mode 1", In-Phase, case [18], the damper motion and the platform damper interaction are governed solely by the platform rotation angle γ_P of Fig. 3. Therefore, forces and displacements at the n_C contact points are dependent on one non-linear parameter only, $q_N(t) \equiv \gamma_P(t)$, that is calculated in the AFT module of Fig. 5b. Forces on platform are reduced to a moment associated to the platform rotation.

Section 2.3

The convergence of the Newton-Raphson zero search takes the form shown Fig. 5a and b. Fig. 5a shows the nesting of the iterative loop in the case of standard procedure valid for the full FEA approach as well as for its PCR version. In the first case the size of the $\mathbf{q}_N^h$ vector is usually of the order of 10^2, already for a harmonic order $h = 1$, due to the fine discretization of contact surfaces both on platform and on damper contact surfaces. For the PCR case the number of DOFs reduces to a maximum of 12, already for a harmonic order $h = 1$, of them 6 for platform and 6 for damper.

Figure 5b shows the nesting of the iterative loop for the PCR case reduced to a plane case thanksto the kinematic properties of Mode 1 during In-Phase forced vibrations. In the case of harmonic order 1, only one DOF is here present, i.e., the amplitude of γ_P^1.

It should be noted that the PCR calculation (either 3D or 2D) can implement MHBM, i.e. with reference to Eq. (1), $H > 1$. This is further shown in Fig. 5a and b. Running a MHBM calculation, however, is not always necessary. In detail, an extended harmonic

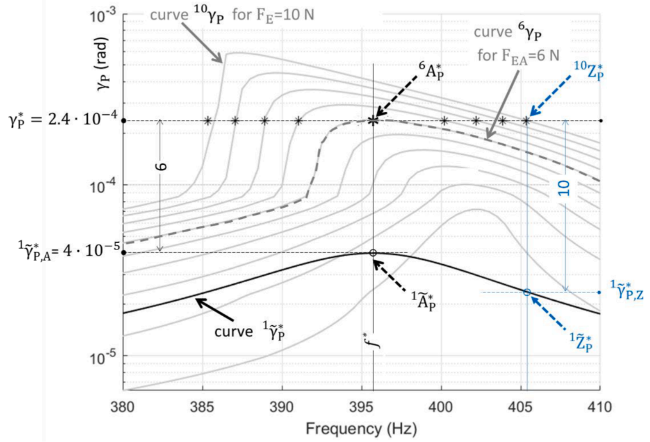

Fig. 7. Light grey curves in background: standard non-linear response curves for $F_E = 1$ to 10 N, step 1. Superimposed example of the Excitation Force Mapping.

support is typically needed to correctly represent contact forces. Since the goal is to compute the first harmonic of the response (i.e. the blade does not present those non-linearities that support super-harmonics), if the correct contact-force cycle shape is available, the problem can be reduced to first order HBM without loss of accuracy. This is possible in all the following cases:

- Full FE or 3D PCR applied to a case with a pre-optimized damper; as demonstrated in [21] using with Direct Time Integration (DTI) results as a benchmark, if the damper is not affected by erratic behaviours (e.g. loss of contact) the harmonic support $h = [0, 1]$ is sufficient to correctly represent contact forces.
- 2D PCR with complementary concept of Base-Cycle (Sect. 2.3); the contact forces on the damper are substituted with the Base Cycle.

The test cases used in the present paper fall within both categories outlined above, therefore a $h = [0, 1]$ harmonic support has been used.

In [16–18] the computational advantages of these progressive reductions have been underlined, the reduction of the number of non-linear variables, and the consequent saving of convergence time and greater efficiency obtained, worth stressing, without loss of accuracy in the calculation of the frequency response under excitation. This is further shown in Fig. 6, where the nonlinear response for Blade A is computed using:

- state-of-the-art full FE calculation (Fig. 5a, [5,10,14,20] as external references).
- 3D PCR (Fig. 5a Sect. 2.1).
- 2D PCR (Fig. 5b, Sect. 2.2 and 2.3).

4. The convergence-free amplitude layered force mapping of the non-linear response

We shall demonstrate here that the non-linear response at given levels of the excitation force is more efficiently obtained by an Amplitude Layered Mapping of the excitation Force, that runs as follows:

4.1. The force mapping procedure

Fig. 7 shows Frequency response curves of the damped blade already presented in [17,18] for the blade (and associated damper) named “blade A” (Appendix A):

- choose a value at will for platform rotation amplitude γ_P^1 in Fig. 4b, ex. $\gamma_P^* = 2.4 \bullet 10^{-4}$rad. In this section the superscript 1, referring to the first harmonic order shall be dropped for brevity.
- identify the corresponding amplitude target layer on Fig. 7.
- take $k^*_{Re} := k_{Re}(\gamma_P^*)$, $k^*_{Im} := k_{Im}(\gamma_P^*)$ valid for such γ_P^*, Fig. 4b.
- by frequency sweep calculate the curve ${}^{1}\sim\gamma_P^*$ of linear (layer-linked) response for unit excitation, $\left|f^1_{EL}\right| = F_E = 1$ N, assuming $\sim k_{Re} = k^*_{Re}$ and $\sim k_{Im}=k^*_{Im}$; this theoretical curve ${}^{1}\sim\gamma_P^*$ has no physical counterpart, because variable displacements imply variable $\sim k_{Re}$ and $\sim k_{Im}$.

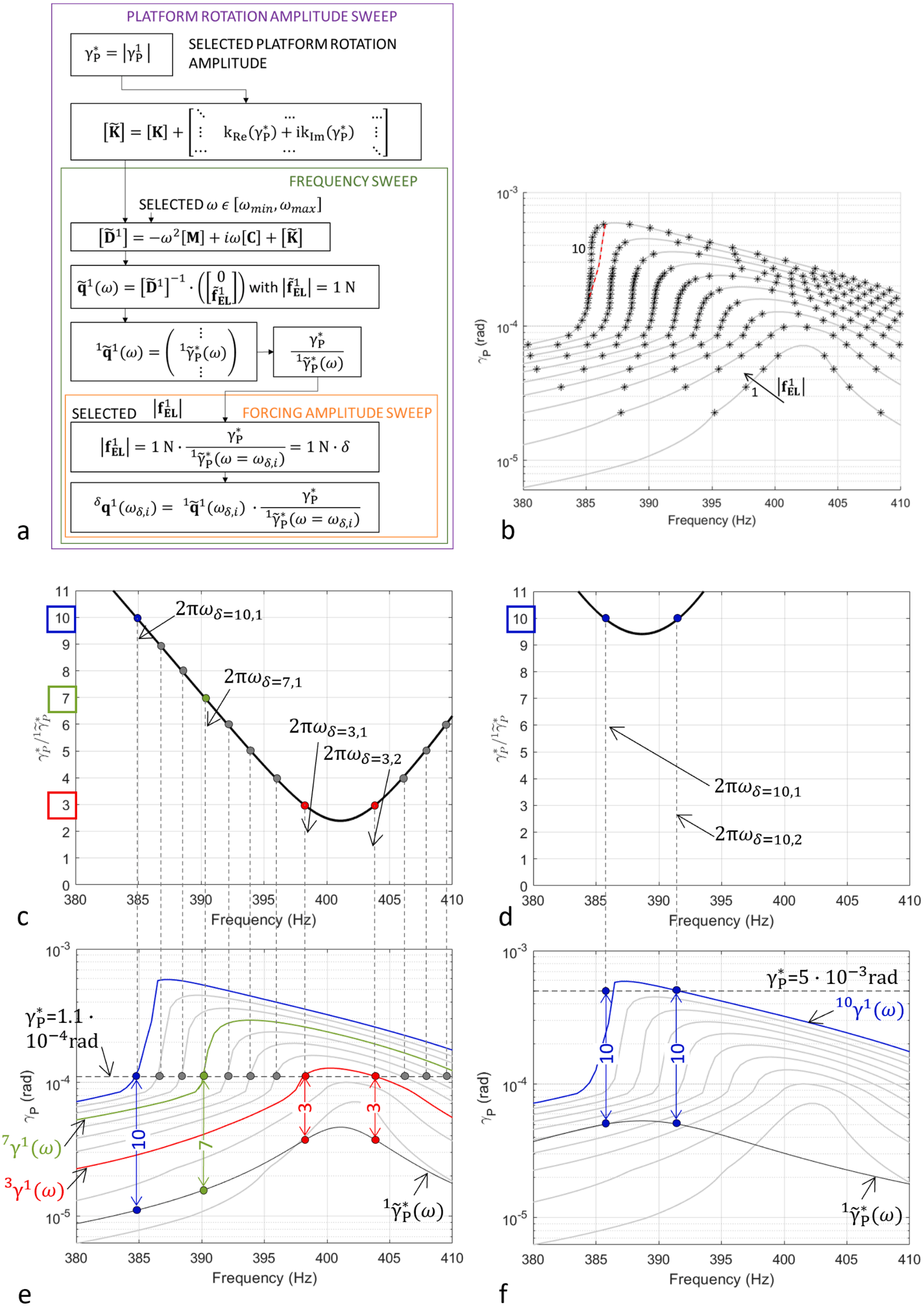

(caption on next page)

Fig. 8. a) Flowchart of the Amplitude Layered (excitation) Force Mapping. b) Points from the Amplitude Layered (excitation) Force Mapping; grey curves in background from the standard convergence method. c-d) Ratio $\frac{\gamma_P^*}{{}^{1}{\sim}\gamma_P^*(\omega)}$ and e-f) Points from the Amplitude Layered (excitation) Force Mapping for $\gamma_P^* = 1.1 \bullet 10^{-4}$ rad, and $\gamma_P^* = 5 \bullet 10^{-3}$ rad respectively.

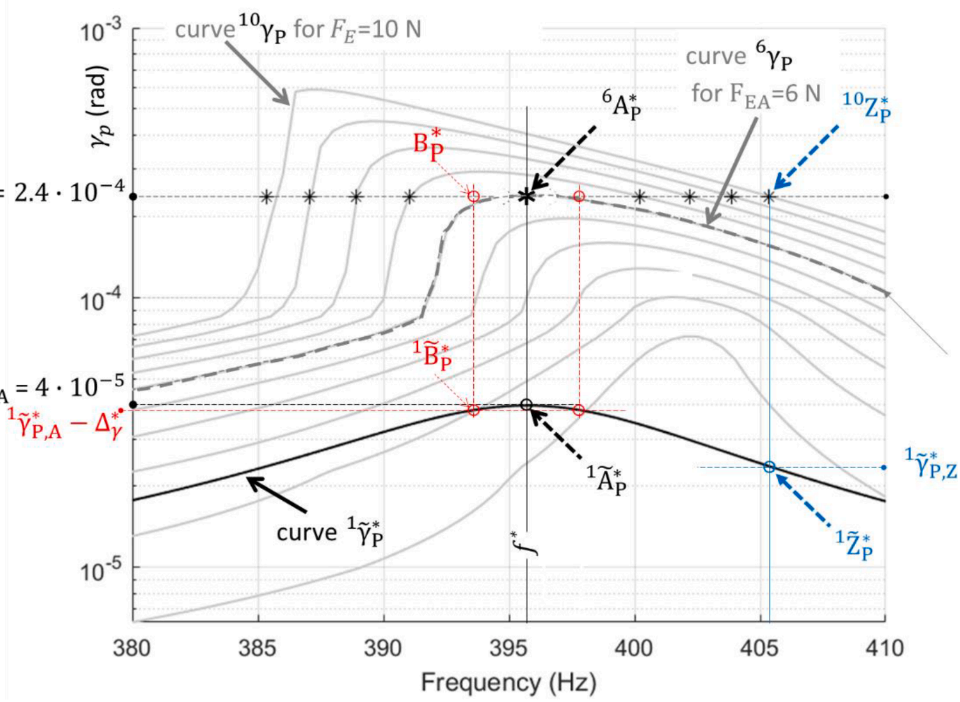

Fig. 9. Correspondence between maxima of the linear (layer linked) unit excitation response and of the non-linear response.

- however, its maximum point ${}^{1}{\sim}A_P^*$ (at the frequency $f^* = \omega^*/2\pi$) has ${}^{1}{\sim}\gamma_{P,A}^* = 4{\cdot}10^{-5}$ rad, then to reach the target layer amplitude $\gamma_P^* = 2.4 \bullet 10^{-4}$rad , point ${}^{6}A_P^*$, it needs an excitation force $F_{EA} = 1\ \text{N}\,\frac{\gamma_P^*}{{}^{1}{\sim}\gamma_{P,A}^*} = \frac{2.4{\cdot}10^{-4}}{4.0\ {\cdot}10^{-5}} = 6$ N.
- in general, any other point, like ${}^{1}{\sim}Z_P^*$, having ordinate ${}^{1}{\sim}\gamma_{P,Z}^*$, needs an excitation $F_{E,Z} = 1\ \text{N}\,\frac{\gamma_P^*}{{}^{1}{\sim}\gamma_{P,Z}^*}$ to find its corresponding point having $\gamma_P = \gamma_P^*$; this can be visualized by taking a vertical distance , equal (Log diagram) to the desired excitation level. For example by selecting a Log 10 vertical distance, we can find, as in the Fig. 7, the point ${}^{1}{\sim}Z_P^*$ such that $\frac{\gamma_P^*}{{}^{1}{\sim}\gamma_{P,Z}^*} = 10$; then the nonlinear response curve for $F_E = 10$ N will pass through point ${}^{10}Z_P^*$.

In practice, the following procedure, also depicted in Fig. 8a, should be performed to obtain the nonlinear forced response for multiple excitation levels shown in Fig. 8b. .

1. Define a series of discrete values for the amplitude of platform rotation γ_P^1.
2. For each one of these discrete values, here termed γ_P^*, retrieve the corresponding $k_{Re}^* := k_{Re}(\gamma_P^*)$, $k_{Im}^* := k_{Im}(\gamma_P^*)$ valid for such γ_P^* , from Fig. 4b.
3. Compute the linear forced response ${}^{1}{\sim}\mathbf{q}^{1}$ for the frequency range of interest $\omega \in [\omega_{min}, \omega_{max}]$:

$$ {}^{1}{\sim}\mathbf{q}^{1} = \left[\sim\mathbf{D}^{1}\right]^{-1} \cdot \left(\begin{bmatrix} 0 \\ \sim\mathbf{f}^{1}_{\mathbf{EL}} \end{bmatrix} \right) \qquad \text{with} \left|\sim\mathbf{f}^{1}_{\mathbf{EL}}\right| = 1\ \text{N} \tag{5} $$

where

$$ \left[\sim\mathbf{D}^{1}\right] = -\omega^2[\mathbf{M}] + i\omega[\mathbf{C}] + \left[\sim\mathbf{K}\right] $$

$$\left[\widetilde{\mathbf{K}}\right] = [\mathbf{K}] + \begin{bmatrix} \ddots & \cdots & \cdots \\ \vdots & k_{\mathrm{Re}}\left(\gamma_{\mathrm{P}}^{*}\right) + ik_{\mathrm{Im}}\left(\gamma_{\mathrm{P}}^{*}\right) & \vdots \\ \cdots & \cdots & \ddots \end{bmatrix} \tag{6}$$

4. Inside the vector ${}^{1}\!\sim\mathbf{q}^{1}(\omega)$, identify the entry corresponding to the platform rotation, here termed ${}^{1}\!\sim\gamma_{\mathrm{P}}^{*}(\omega)$. Such response is represented in the lower part of Fig. 8e and f for $\gamma_{\mathrm{P}}^{*} = 1.1 \bullet 10^{-4}$ rad, and $\gamma_{\mathrm{P}}^{*} = 5 \bullet 10^{-3}$ rad, respectively.
5. Compute the curve $\frac{\gamma_{\mathrm{P}}^{*}}{{}^{1}\!\sim\gamma_{\mathrm{P}}^{*}(\omega)}$, two examples are shown in Fig. 8c and d for $\gamma_{\mathrm{P}}^{*} = 1.1 \bullet 10^{-4}$ rad, and $\gamma_{\mathrm{P}}^{*} = 5 \bullet 10^{-3}$ rad, respectively.
6. The ratio $\frac{\gamma_{\mathrm{P}}^{*}}{{}^{1}\!\sim\gamma_{\mathrm{P}}^{*}(\omega)}$ at a given frequency ω, represents the scaling factor that, if multiplied by ${}^{1}\!\sim\mathbf{q}^{1}(\omega)$ will yield the response ${}^{\delta}\!\sim\mathbf{q}^{1}(\omega)$ valid for a forcing level $\delta = \frac{\gamma_{\mathrm{P}}^{*}}{{}^{1}\!\sim\gamma_{\mathrm{P}}^{*}(\omega)}$ 1 N.
7. On the $\left(\omega, \frac{\gamma_{\mathrm{P}}^{*}}{{}^{1}\!\sim\gamma_{\mathrm{P}}^{*}(\omega)}\right)$ plot (Fig. 8c and d), identify the frequency(ies) $\omega_{\delta,i}$ for which the ratio $\frac{\gamma_{\mathrm{P}}^{*}}{{}^{1}\!\sim\gamma_{\mathrm{P}}^{*}(\omega=\omega_{\delta i})}$ is equal to the forcing level δ of interest. In the present case, the goal is to reproduce the forcing levels $\left|\mathbf{f}_{\mathrm{EL}}^{1}\right|$ equal to integers spanning 1 to 10. Depending on the amplitude of platform rotation γ_{P}^{*} being investigated, the ratio $\frac{\gamma_{\mathrm{P}}^{*}}{{}^{1}\!\sim\gamma_{\mathrm{P}}^{*}(\omega)}$ may assume different values for the frequency range of interest. In the case represented in Fig. 8c, $\delta = [3, 4, 5, 6, 7, 8, 9, 10]$ are present, while for the case in Fig. 8d, only $\delta = 10$ is present within the investigated frequency range.
8. For each δ of interest, and for each identified $\omega_{\delta,i}$, the nonlinear response at forcing level $\left|\mathbf{f}_{\mathrm{EL}}^{1}\right| = \delta \bullet 1$ N and at frequency $\omega_{\delta,i}$ can be obtained as

$$ {}^{\delta}\mathbf{q}^{1}\left(\omega_{\delta,i}\right) = {}^{1}\!\sim\mathbf{q}^{1}\left(\omega_{\delta,i}\right) \cdot \frac{\gamma_{\mathrm{P}}^{*}}{{}^{1}\!\sim\gamma_{\mathrm{P}}^{*}\left(\omega_{\delta,i}\right)} \tag{7}$$

The entries inside vector ${}^{\delta}\mathbf{q}^{1}\left(\omega_{\delta,i}\right)$ corresponding to the platform rotation, i.e. ${}^{\delta}\gamma^{1}\left(\omega_{\delta,i}\right)$, are shown by means of color-coded dots in Fig. 8e and f. It should be noted that.

- all the dots lie on the horizontal line corresponding to the γ_{P}^{*} level chosen at Step 2.
- the vertical distance on the Log diagram between the dot located on the ${}^{\delta}\gamma^{1}\left(\omega_{\delta,i}\right)$ curve and the corresponding one on the ${}^{1}\!\sim\gamma_{\mathrm{P}}^{*}$ curve is equal to δ.

The procedure described at steps 7–8 can be repeated for any available forcing level $\left|\mathbf{f}_{\mathrm{EL}}^{1}\right| = \delta \bullet 1$ N of interest and the complete procedure (steps 2–8) may then be repeated for any convenient selection of γ_{P}^{*} levels: the values of the excitation forces are mapped onto each level (as in Fig. 8e and f for Mapping for $\gamma_{\mathrm{P}}^{*} = 1.1 \bullet 10^{-4}$ rad, and $\gamma_{\mathrm{P}}^{*} = 5 \bullet 10^{-3}$ rad respectively), then all levels mapped onto the whole (f, γ_{P}) plane. The method allows to track, layer by layer of γ_{P}^{*} amplitude, the response for a chosen set of excitation levels $\left|\mathbf{f}_{\mathrm{EL}}^{1}\right|$. The frequency $\omega_{\delta,i}$ of the points which are used to construct the curves is a by-product of the selection of the γ_{P}^{*} and $\left|\mathbf{f}_{\mathrm{EL}}^{1}\right|$ parameters. Nevertheless, an appropriate sweep of both of these parameters guarantees a fine characterization of the the response curves, as shown in Fig. 8b where the points are from excitation Force Mapping, while the grey curves in the background come from the standard convergence method.

A close examination of Fig. 8b, curves for $\mathrm{F_E} = 9, 10$ N shows that where convergence of the standard method failed (dashed red section), in the vicinity of the steepest ramp (see also Fig. 7), the Amplitude Layered (excitation) Force Mapping was able to get fine results.

4.2. – Tracing the backbone of nonlinear response curves

It is shown here that the maxima of the (non-linear) response curves at assigned exciting force are generated by mapping maxima of the linear (layer-linked) response curves for unit excitation. Steps are:

- the linear response curve ${}^{1}\!\sim\gamma_{\mathrm{P}}^{*}$ is convex upwards, with a maximum in ${}^{1}\!\sim\mathrm{A}_{\mathrm{P}}^{*}$.
- its intersection with a level ${}^{1}\!\sim\gamma_{\mathrm{P,B}}^{*} = {}^{1}\!\sim\gamma_{\mathrm{P,A}}^{*} - \Delta_{\gamma}^{*}$, lower than ${}^{1}\!\sim\gamma_{\mathrm{P,A}}^{*}$, determines two points like ${}^{1}\!\sim\mathrm{B}_{\mathrm{P}}^{*}$.
- the corresponding point $\mathrm{B}_{\mathrm{P}}^{*}$ on amplitude level γ_{P}^{*} requires an excitation force $\mathrm{F_{E,B}} = 1\ \mathrm{N} \cdot \frac{\gamma_{\mathrm{P}}^{*}}{{}^{1}\!\sim\gamma_{\mathrm{P,A}}^{*} - \Delta_{\gamma}^{*}}$.
- then all excitation forces of points at amplitude level γ_{P}^{*} are $\mathrm{F_{E,B}} > \mathrm{F_{E,A}}$.

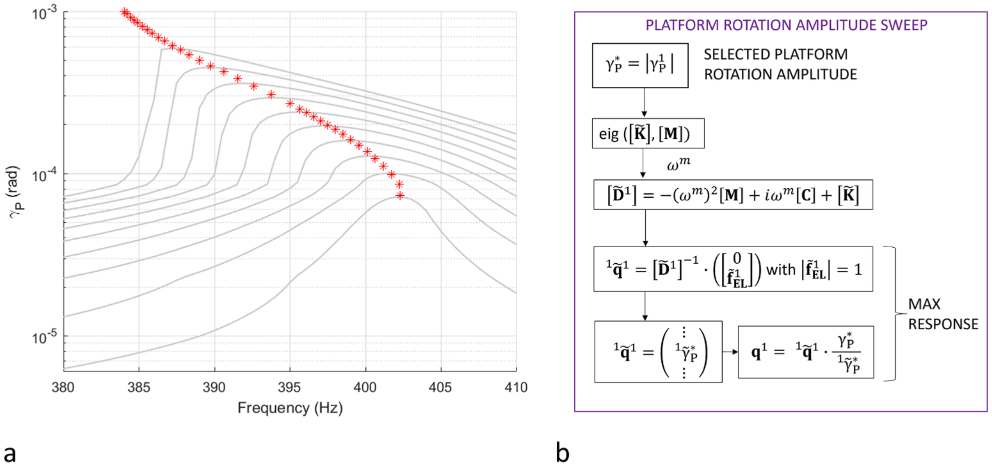

Fig. 10. a) dots: direct calculation of the backbone points of the nonlinear response. curves in background: reminder of the full non-linear response curves. b) flowchart of the direct calculation of the non-linear response backbone curve, based on eigenvalues.

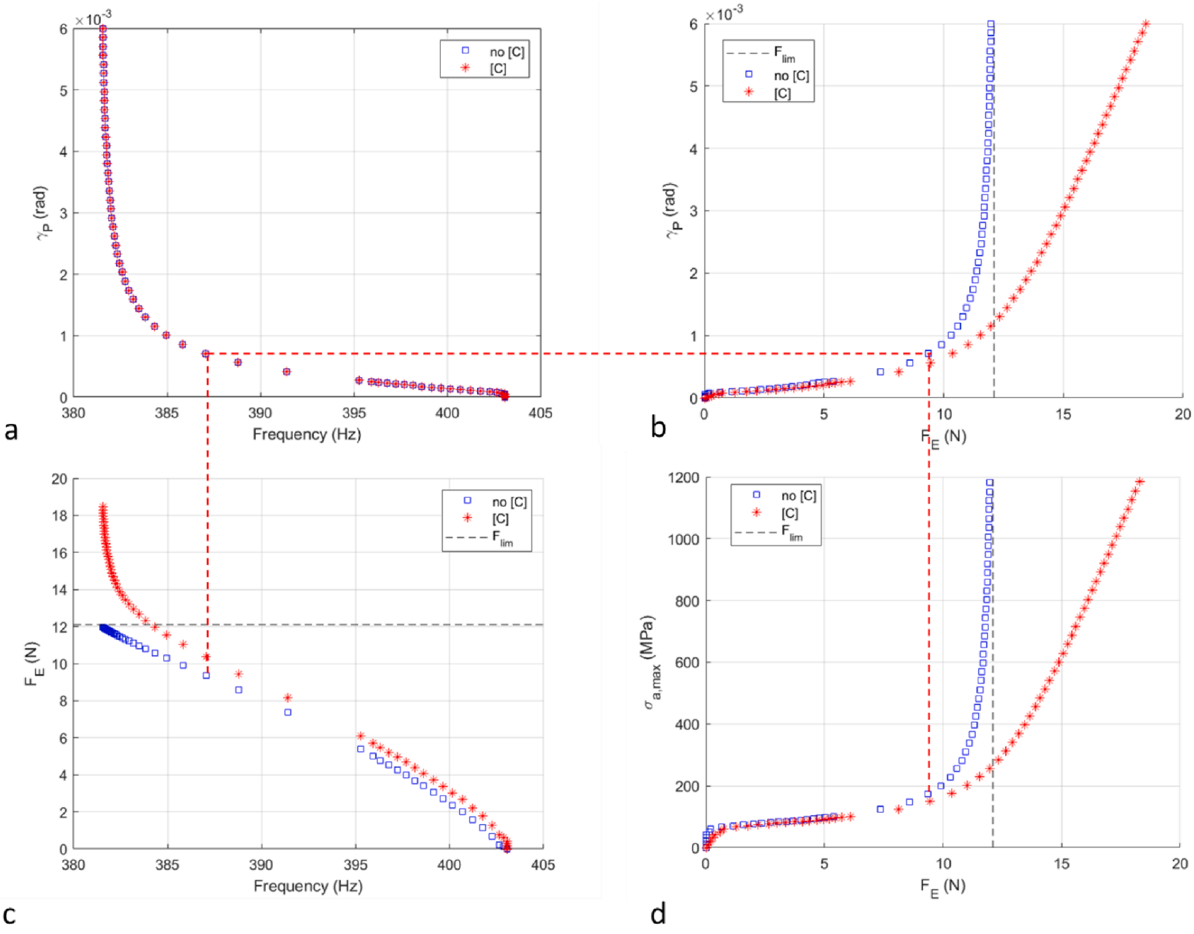

Fig. 11. a) platform rotation amplitude vs. frequency, b) platform rotation amplitude vs. “proof” excitation force, c) “proof” excitation force vs. resonance frequency, d) peak stress amplitude at the airfoil-platform junction vs. “proof” excitation force at resonance frequency.

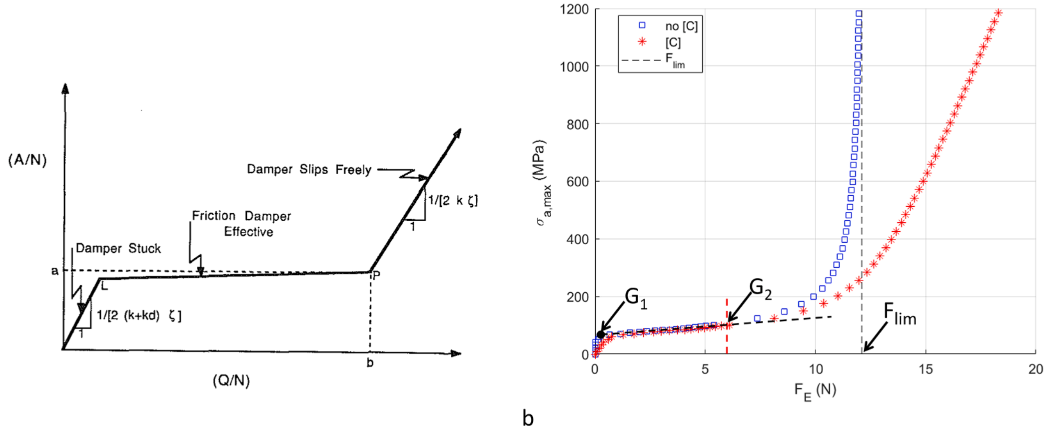

Fig. 12. a) The amplitude-normalized form of damper performance curve from [25]. b) The coupled damper performance curve for airfoil "witness" maximum stress amplitude (GG design diagram).

- it follows that the curve at excitation $\mathrm{F}_{\mathrm{E,A}}$ has only one common point with, i.e. is tangent to the level γ_{P}^{*} in ${}^{6}\mathrm{A}_{\mathrm{P}}^{*}$.
- points $\overset{1}{\sim}\mathrm{A}_{\mathrm{P}}^{*}$ and ${}^{6}\mathrm{A}_{\mathrm{P}}^{*}$ have the same frequency f^*.
- this demonstrates that the maxima of the F_{E} curves (backbone) can be calculated as the transformation of maxima of the linear (layer-linked) response curves.
- it is evident that being able to predict the frequency of the maximum of each $\overset{1}{\sim}\gamma_{\mathrm{P}}^{*}$ curve, valid for different values of platform rotation γ_{P}^{*}, provides a shortcut to obtaining the backbone of the forced response curves.
- then the maxima, dots in Fig. 10a, can, alternatively, be calculated based on eigenvalues as shown in Fig. 10b, without need to calculate the response curves.

5. Example of application: A case study

As was already presented in [17,18], by means of the modal form of the damper undamped blade on the platform, and in the absence of modal damping, the (exciting) Limit Force $\mathrm{F}_{\mathrm{lim}}$ is calculated, at which the amplitude of the response becomes infinite. A "proof" excitation force F_{E} is applied at the airfoil mid-length point E, orthogonally to the longer dimension of neck, platform, and damper.

Fig. 11a – d show the analogues already presented in [17,22], but recalculated with the method introduced here. In the comparison, the greater fineness with which curves can be plottedwith the new method is evident, indicative of the incomparable ease made possible by the elimination of convergence problems.

In addition, the diagrams provide curves both with zero structural (modal) damping and with a modal damping equivalent to some 0.2 % on a full FEM model.

The correspondence between the diagrams in Fig. 11b and the "*idealized response curve*" referred to in [25] as the "*damper performance curve*", Fig. 12a, first introduced in that article for a blade-to-ground damper, is evident. The blade tip vibration amplitude was A, the friction normal load was N, the magnitude of harmonic excitation on blade (shaker table) was Q. In [25] it was pointed out that while "*at the low end of the response curve, the friction damper is stuck, since the excitation is too small to cause it to slip, and the response is linear*", while "*at the high end of the curve, the large excitation causes the friction damper to slip freely and the response is linear again*", in the middle section "*friction damping controls the response, rendering viscous damping effects negligible*". It must be acknowledged that [25] suggests that blade response should be monitored in terms of either tip amplitude or (although not shown) stress levels. The concept is illustrated also in otherpapers such as [25,26,27].

The elbows of the curves in Fig. 11 suggest the identification of a "conventional" slope endpoint along which dry damping controls the vibration amplitude. Their shape heuristically supports the proposal [17,18] to consider 50 % of the limit force as the admissible "proof" excitation force, point G_2. As in [20,25,26,27], this work focuses on vibrational aspects and therefore assumes that the blade design is limited by HCF safety issues. Particular attention is therefore given to the maximum amplitude of alternating stresses during vibration, Fig. 11d, which in this work is considered at a "witness" cross-section, considered to be that of the profile-platform junction. However, depending on the geometry of the blade and the magnitude of the damper-platform interaction (i.e., anywhere between full-stick and full-slip), the stress peak can occur either at the witness cross-section or at the neck [20,26], e.g., near the fillet area near the first lobe of the fir tree, as in [20]. In [26] a purposely defined parameter keeps track of the maximum-to-witness stress ratio.

Fig. 12b is the damper performance curve for the case here studied, however in terms of max "witness" stress amplitude vs. "proof" excitation force amplitude. In both cases, 12.a,b the damper-blade matching criterion is that the specified maximum response must be less than some specified limit value for the largest possible excitation force. This "GG design diagram" is an evolution of the damper performance curve, however in terms of maximum alternating stress amplitude in a witness cross-section as indicated in [20,26,27], however with some important differences:

- G_1 corresponds now to the “Base-Cycle” [12,18].
- G_2 is the “conventional” (safe) admissible point [16,18], at a suitable fraction (here, 50 %) of F_{lim}.
- F_{lim} is the dry-friction limit exciting force, in the absence of any viscous-like structural damping, calculated according to [16,17,18].

The HCF safety criterion materializes as the couple of constraints:

$$F_E(G_2) \leq 0.5F_{lim} \tag{8a}$$

$$\sigma_{a,max} \leq \sigma_{a,all} \tag{8b}$$

where $\sigma_{a,all}$ (not represented in Fig. 12b) is the allowable (fatigue) alternating stress amplitude of the material, considering temperature, mean tensile centrifugal stress, notch stress concentration. In [26] this value is estimated between 50 and 100 MPa “*from the statistical data available for a typical class of turbine blades*”; in [17] it was estimated at about 80 MPa.

A practical evaluation of the numerical benefits to be obtained from the progressive reduction of numerical effort was carried out using the case study examined here [17,18].

A comparative estimate is obtained by observing the number of non-linear n_{DOF} and the number of iterative calculation n_{ITER} required to achieve convergence on a single (ω, F_E) selection:

1. Standard (3D): the standard procedure of Fig. 5a is taken as a reference, with a number of DOFs on platform and damper equal to the minimum necessary to simulate contact, i.e., around 50 in [13,17,18] (worth to be noticed that they would be one order of magnitude higher in the so-called high-fidelity approach [6,10,14])
2. PCR (3D): (again Fig. 5a) the non-linear n_{DOF} size of the system is reduced to 12–25 % of the Standard 3D; in addition, the smaller system reduces the n_{ITER} number of iterations for each convergence cycle to 30-50 %.
3. PCR + Base-Cycle (2D): (Fig. 5b) the n_{DOF} size of the system is reduces to 1–2 % of the Standard 3D; in parallel, the number of n_{ITER} iterations for each convergence cycle is reduced to 10 %, on average for the cases examined.
4. PCR + Base-Cycle + conv.-free (2D): (Fig. 8a) again $n_{DOF} = 1$–2 %, however, depending on the number of amplitude layers and the number of frequency steps the computing time is reduced between 0.5 % and 1.5 % compared to the Standard 3D; finally, with the backbone approach, the computing time reduces to an absolute minimum.

Moreover, methods 2, 3 are affected by convergence problems for excitation forces over 80 % of the limit force, method 1 for even lower values.

All this can be better appreciated in the context of the effort required to build the GG design diagram. With methods 1 to 3, and after developing some experience, the procedure is to be repeated for at least 10 values of excitation F_E and around 20 values of frequency ω to find shape and maximum of the response curve, so 10*20 nonlinear (ω, F_E) selections. With method 4, especially if in addition the backbone procedure of Fig. 10b is employed finding the eigenvalue and going directly to the maximum, the computational cost is really negligible, boiling down to calculating the eigenvalues of a small system for some 15–20 values of γ_P that cover the investigation needs.

In terms of computing time, this operation is equal to (perhaps even less than) just one of the convergence steps for a single (ω, F_E) selection of methods 2, 3. In fact with Newton-Raphson convergence (methods 1, 2, 3) one of the ways to get an initial guess for the first frequency value investigated is to use the stick mode of the structure, so the eigenvalues/vectors need to be calculated there too. Then, with methods 1, 2, 3 the calculation of the eigenvalues is a very small initial burden, insignificant if compared to the total.

With method 4, implemented with the backbone curve, this is about 90 % of the computational effort, Fig. 10a.

6. Conclusions

A method was introduced to determine response curves in a non-linear case with assigned exciting forces, avoiding convergence cycles and the associated Jacobian calculation.

The scope, of great practical interest, examined here is to find the most advantageous coupling between a UD and a turbine blade.

The method is applied in the case of the blade-damper system described with the PCR (Platform Centred Reduction), further reduced to a single DOF, i.e. the bending rotation of the platform, without substantial reduction in accuracy, in the case of Mode 1 (bending) and In-Phase vibrations. In this case, the mechanical actions of the damper on the platform are reduced to a complex stiffness. The real and imaginary values of this stiffness are functions of the absolute rotational amplitude of the platform, functions calculated for the damper alone, i.e. separately and before undertaking anycalculation of coupling with the damper.

With this method, which may be briefly described as "Amplitude Layered (excitation) Force Mapping", the linear response under a unit force is calculated for a complex stiffness corresponding to a given level of platform rotation. Then, a proportional transformation directly calculates the excitation force values that produce that given level of rotation in the full slip-full stick range. Once these excitation values have been mapped for the given level of rotation, and the calculation layered for the desired levels, non-linear response curves with assigned excitatory force are constructed.

With this procedure, it is then possible to obtain these curves by avoiding the convergence process involving the Newton-Raphson

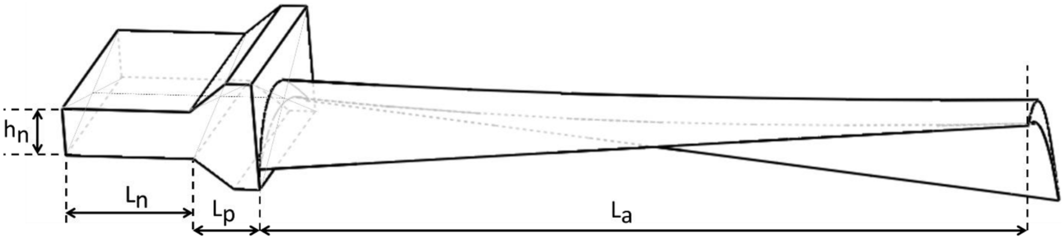

Fig. A1. "blade A" from [17].

solution in the standard method..

The proposed method has been described in its general principles, and then applied to a realistic example of a damper-blade system already used in previous works by the same authors, so as to allow a comparison between the standard method (with convergence) and the new one (convergence-free) proposed here for the first time.

The diagrams show the "damper performance curve" however in the form preferred in this work, i.e. highlighting the alternating fatigue stress levels at the most stressed points as a function of the exciting force, for the purposes of a blade design that is limited by HCF safety issues. The much greater accuracy of the diagrams obtainable with the method here proposed over the standard one is evident.

With concrete reference to a realistic blade already introduced in previous works, of which this is a completion, it was estimated that switching from the standard method to the PCR method allowed for a reduction of the numerical load of the solution for the single (ω, F_E) selection by two orders of magnitude, then up to three orders of magnitude if the "Base-Cycle" (Mode 1, In-phase) method is implemented in the PCR.

With the adoption of this novel convergence-free method, the computational effort is reduced to a hitherto unprecedented minimum.

In the context of calculating damper performance curves for blade-to-damper coupling, this extreme, computational efficiency allows DOE or parametric analysis to be reconsidered as a competitive alternative to surrogate models when optimizing damper shape and size or when assessing the impact of uncertainties in geometric and contact parameters.

To complete the picture, the aim of the proposed method is not to replace full FEA calculations, but rather to employ them downstream of the numerically intensive part of the process where the method proposed here is most efficient, thus reserving the use of FEA for the final design, certification and study of the influence of the dampers on the blades in cases other than Mode 1 and In-Phase.

Declaration of competing interest

The authors declare that they have no known competing financial interests or personal relationships that could have appeared to influence the work reported in this paper.

Data availability

Data will be made available on request.

Appendix A

Fig. A1 illustrates the main data of blade and damper, [16].

$h_n = 8$ mm, $L_n = 20$ mm, $L_p = 10$ mm, $L_a = 120$ mm.

- damper centrifugal force: 900 N.
- 44 blades stage disk, 350 kW per stage, 7.9 kW per blade.
- disk rotating at: $\Omega = 6000$ rpm.
- mean (static) circumferential design blade force component: 60 N.
- mean static lift design force on the blade: 73 N.
- operating temperature: 650 °C.
- $\mu = 0.3$ friction coefficient.

References

[1] S. Filippi, A. Akay, M.M. Gola, Measurement of Tangential Contact Hysteresis During Microslip, ASME J. Trib. (2004) 482–489, https://doi.org/10.1115/1.1692030.

[2] Botto, D, Lavella, M, & Gola, MM. "Measurement of Contact Parameters of Flat on Flat Contact Surfaces at High Temperature." *Proc. ASME Turbo Expo 2012 – Volume 7: Structures and Dynamics",* Copenhagen, Denmark. June 11–15, 2012. pp. 1325-1332 https://doi.org/10.1115/GT2012-69677.

[3] M.M. Gola, T. Liu, A direct experimental numerical method for investigations of a laboratory underplatform damper behavior, Int. J. Solids Struct. 51 (25–26) (2014) 4245–4259, https://doi.org/10.1016/j.ijsolstr.2014.08.011.

[4] C. Gastaldi, T. Berruti, M.M. Gola, A novel test rig for friction parameters measurement on underplatform dampers, Int. J. Solids Struct. 185–186 (2020) 170–181, https://doi.org/10.1016/j.ijsolstr.2019.08.030.

[5] L. Pesaresi, L. Salles, A. Jones, J.S. Green, C.W. Schwingshackl, Modelling the nonlinear behaviour of an underplatform damper test rig for turbine applications, Mech. Sys. Signal Proc. 85 (2017) 662–679, https://doi.org/10.1016/j.ymssp.2016.09.007.

[6] L. Pesaresi, J. Armanda, C.W. Schwingshackl, L. Salles, C. Wong, C., An advanced underplatform damper modelling approach based on a microslip contact model, J. Sound Vib. 436 (8) (2018) 327–340, https://doi.org/10.1016/j.jsv.2018.08.014.

[7] Y. Yuan, A. Jones, R. Setchfield, C. Schwingshackl, Robust design optimisation of underplatform dampers for turbine applications using a surrogate model, J. Sound Vib. 494 (6) (2020) 115528, https://doi.org/10.1016/j.jsv.2020.115528.

[8] Denimal, E., El Haddad, F., Wong, C., and Salles, L., Topological Optimisation of Under-Platform Dampers With Moving Morphable Components and Global Optimisation Algorithm for Nonlinear Frequency Response, ASME. *J. Eng. Gas Turbines Power.* February 2021; 143(2): 021021 https://doi.org/10.1115/1.4049666.

[9] S. Hu, H. She, G. Yang, C. Zang, C. Li, The Influence of Interface Roughness on the Vibration Reduction Characteristics of an Under-Platform Damper, Appl. Sci. 13 (2023) 2128, https://doi.org/10.3390/app13042128.

[10] L. Panning, K. Popp, W. Sextro, F. Goetting, A. Kayser, I. Wolter, Asymmetrical underplatform dampers in gas turbine bladings: Theory and Application, ASME Paper GT2004-53316, Proc. of ASME Turbo Expo, Vienna, Austria 2004, https://doi.org/10.1115/GT2004-53316.

[11] M. Bobo, United States Patent N. 5,156,528, Vibration damping of gas turbine engine buckets, Inventor Melvin Bobo, General Electric (1992).

[12] M.M. Gola, A general geometrical theory of turbine blade underplatform asymmetric dampers, Mechanical Systems and Signal Processing, Vol. 191 (2023) 110167 – online 2023.02.20, https://doi.org/10.1016/j.ymssp.2023.110167.

[13] C. Gastaldi, T. Berruti, M.M. Gola, The Effect of Surface Finish on the Proper Functioning of Underplatform Dampers, J. Vib. Acoust. 142 (5) (2020), 051103, https://doi.org/10.1115/1.4046954.

[14] A. Fantetti, R. Setchfield, C. Schwingshackl, Nonlinear dynamics of turbine bladed disk with friction dampers: Experiment and simulation, Int. Jour. Mech. Sci. 257 (1) (2023) 108510, https://doi.org/10.1016/j.ijmecsci.2023.108510.

[15] C. Gastaldi, T.M. Berruti, A method to solve the efficiency-accuracy trade-off of multi-harmonic balance calculation of structures with friction contacts, Int. J. Non-Linear Mech 92 (March 2017), https://doi.org/10.1016/j.ijnonlinmec.2017.03.010.

[16] C. Gastaldi, M.M. Gola, Platform Centered Reduction: A Process Capturing the Essentials for Blade-Damper Coupled Optimisation, ASME Journal of Engineering for Gas Turbines and Power 143 (8) (2021) 081001, https://doi.org/10.1115/1.4049187.

[17] C. Gastaldi, M.M. Gola, A Method to Minimize the Effort for Damper-Blade Matching Demonstrated on Two Blade Sizes, Appl. Sci. 11 (2021) 5171, https://doi.org/10.3390/app11115171.

[18] C.Gastaldi, M.M. Gola, Non-Linear Damper-Blade Coupling Calculations Reduced to Essentials, J. Eng. Gas Turbines Power 145(2) (2023) 021016 , Paper No: GTP-22-1427, Online: November 29, 2022, https://doi.org/10.1115/1.4055414.

[19] M. Krack, S. Tatzko, L. Panning-von Scheidt, J. Wallaschek, Reliability optimisation of friction-damped systems using nonlinear modes, J. Sound Vib. 333 (2014) 2699–2712, https://doi.org/10.1016/j.jsv.2014.02.008.

[20] M. Hüls, L.P. von Scheidt, J. Wallaschek, Influence of Geometric Design Parameters onto Vibratory Response and HCF Safety for Turbine Blades with Friction Damper, J. Eng. Gas Turbines Power 141 (4) (July 2018), https://doi.org/10.1115/1.4040732.

[21] C. Gastaldi, T.M. Berruti, M.M. Gola, The Relevance of Damper Pre-Optimisation and Its Effectiveness on the Forced Response of Blades, ASME. J. Eng. Gas Turbines Power 140 (6) (2018), 062505, https://doi.org/10.1115/1.4038773.

[22] C.Gastaldi, M.M. Gola, Design Tools to the Best Coupling of Dry-Friction Solid Underplatform Dampers to Turbine Blades, *Proc. of the ASME Turbo Expo 2019: Turbomachinery Technical Conference and Exposition",* Volume 7B: Structures and Dynamics. Phoenix, Arizona, USA. (2019) V07BT35A014, https://doi.org/10.1115/GT2019-91040.

[23] C. Gastaldi, T.M. Berruti, Competitive Time Marching Solution Methods for Systems with Friction-Induced Nonlinearities, Appl. Sci. 8 (2) (2018) 291, https://doi.org/10.3390/app8020291.

[24] M. Berthillier, C. Dupont, R. Mondal, J.J. Barrau, Blades forced response analysis with friction dampers, J. Vib. Acoust. 120 (2) (1998) 468–474, https://doi.org/10.1115/1.2893853.

[25] T.M. Cameron, J.H. Griffin, R.E. Kielb, T.M. Hoosac, An Integrated Approach for Friction Damper Design, ASME. J. Vib. Acoust. 112 (2) (1990) 175–182, https://doi.org/10.1115/1.2930110.

[26] R.K. Giridhar, P.V. Ramaiah, G. Krishnaiah, S.G. Barad, Gas Turbine Blade Damper Optimisation Methodology, Advances in Acoustics and Vibration, Volume 2012, Article ID 316761, 13 pages, https://doi.org/10.1155/2012/316761.

[27] J. Szwedowicz, High Cycle Fatigue, Notes on Structural Design of Aircraft, Engines. NATO OTAN. (2012), https://doi.org/10.14339/RTO-EN-AVT-207.